GEOPHYSICS, VOL. 79, NO. 5 (SEPTEMBER-OCTOBER 2014); P. R221–R232, 12 FIGS., 3 TABLES.
10.1190/GEO2013-0372.1

Bayesian inversion for effective pore-fluid bulk modulus based on fluid-matrix decoupled amplitude variation with offset approximation

Xingyao Yin[1] and Shixin Zhang[2]

ABSTRACT

Fluid indicators estimated from seismic data play important roles in reservoir characterization and prospect identification. Traditionally, there are a variety of fluid indicators proposed, but they are very likely to provide ambiguous results for fluid identification due to the fact that their sensitivity is dependent upon the mixed effect of pore fluid and rock porosity. To raise the sensitivity of fluid indication, we used the effective pore-fluid bulk modulus as a fluid indicator. Starting with the poroelastic amplitude variation with offset (AVO) theory and the corresponding rock-physics model with the homogeneous sorting trend, we derived a new AVO approximation that allowed us to estimate the effective pore-fluid bulk modulus in a direct fashion. The inversion for the fluid indicator is formulated in Bayesian framework with the Cauchy distribution as a prior constraint. We tested the method on synthetic data and analyzed the feasibility and stability of the inversion. A field data example shows that the effective pore-fluid bulk modulus can reduce the ambiguity caused by the rock porosity and improve the quality of fluid discrimination in a clastic reservoir. Further research needs to be done on the reservoirs that do not fit the rock-physics model without a sorting trend.

INTRODUCTION

Fluid indicators estimated from seismic data can be used to identify pore fluids and validate hydrocarbon prospects. Actual experience with dry holes drilled on prospects has demonstrated that one of the major challenges we face is how to reduce the uncertainties in reservoir fluid discrimination. Usually, there are two major factors which may degrade the quality of reservoir fluid identification. First, the fluid indicators may not be sensitive to the local reservoir pore-fluid types. Second, the elastic parameters estimated through a seismic inversion scheme may have poor reliability, which further reduces the accuracy of the estimated fluid indicators. This paper is concerned with the inversion of a sensitive fluid indicator, which can potentially increase the reliability of reservoir prediction.

Seismic amplitude anomalies have been used as hydrocarbon indicators for many years, using techniques such as bright spots, dim spots, and flat spots, etc. With the advent of exploration toward more and more lithologic reservoirs, simple qualitative methods are no longer good techniques for identifying hydrocarbon detection. Recently, direct rock property estimation from seismic data appears to provide a better way to discriminate different pore-fluid types. The quantitative fluid indicator was first defined as a weighted difference between P and S reflectivities (Castagna et al., 1985; Smith and Gidlow, 1987; Gidlow et al., 1992; Fatti et al., 1994; Gray et al., 1999; Dillon et al., 2003). With the development of prestack seismic inversion, the definition of the fluid indicator has been extended into the impedance domain, where P- and S-wave impedances ($I_P = \rho V_P$ and $I_S = \rho V_S$) are the main parameters used to construct fluid indicators. Goodway et al. (1997) propose $\lambda\rho$ and $\mu\rho$ as fluid indicators, where $\lambda\rho = I_P^2 - 2I_S^2$ and $\mu\rho = I_S^2$. Zhou and Hilterman (2010) show the advantage of $\lambda\rho$ and $\mu\rho$ (as crossplots or ratios) in fluid discrimination. Russell et al. (2003) generalize $\lambda\rho$ to the attribute $I_P^2 - cI_S^2$, where $c = (V_P/V_S)^2_{dry}$, which can be used as a general expression of fluid indicator. Quakenbush et al. (2006) propose Poisson's impedance PI, where $PI = I_P - cI_S$ and c are the weighting factor. Russell et al. (2011) use the Gassmann fluid/porosity term f as the fluid indicator, where f is the difference between the saturated and dry bulk modulus. However, these fluid indicators are very likely to provide ambiguous results for fluid identification due to the fact that their sensitivity is dependent upon the mixed effect of pore fluid and rock porosity (Zhang et al., 2010). To improve the sensitivity of fluid indication, we present the effective pore-fluid bulk modulus as a new fluid indicator that is only related to the pore fluid and thus minimizes the rock-matrix effect in an ideal case. Based on the work of Russell et al. (2011), we combine a rock-physics empirical formula and poroelastic amplitude variation with offset (AVO) theory to generate

Manuscript received by the Editor 4 October 2013; revised manuscript received 5 May 2014; published online 21 August 2014.
[1]China University of Petroleum, Qingdao, China. E-mail: yinxingyao62@163.com.
[2]CNOOC Research Institute, Beijing, China. E-mail: zsxvegata@126.com.

a new linearized AVO approximation, which contains the effective pore-fluid bulk modulus. And based on the new AVO approximation, the effective pore-fluid bulk modulus in the seismic scale is estimated through seismic inversion.

Seismic inversion is an important intermediate step in rock-properties estimation and reservoir-fluid identification. In terms of practicality and efficiency, AVO inversion is one of the most commonly used techniques. AVO inversion itself is an ill-conditioned problem. Because the quality of the inversion will have a large impact on hydrocarbon evaluation, the inversion methodology used is very important. The Bayesian approach takes advantage of the observed data with the available prior information as the constraint, and can stabilize the inversion process (Buland and Omre, 2003; Downton, 2005; Alemie and Sacchi, 2011). The inversion scheme, we present here is motivated by the work of Downton (2005). We formulate the inversion of the effective pore-fluid bulk modulus and other associated elastic parameters in a Bayesian framework by assuming that the likelihood model has a Gaussian probability distribution, and we use the Cauchy distribution as a prior model to regularize the inversion procedure. This leads to sparse solutions of effective pore-fluid bulk modulus and the other parameters.

In summary, this paper proposes a Bayesian AVO inversion method for the effective pore-fluid bulk modulus. The effective pore-fluid bulk modulus can be used as a fluid indicator, and can diminish the ambiguity caused by rock-matrix factors, especially porosity. We start by reexpressing the Russell et al. (2011) approximation based on poroelastic theory and other rock-physics theories (Nur et al., 1998; Han and Batzle, 2003). Using the fluid-matrix decoupled AVO approximation, we then give a mathematical description of our Bayesian inversion scheme. A synthetic inversion test follows, and then we demonstrate the applicability of our method with a real example in the Bo Sea.

FLUID-MATRIX DECOUPLED AMPLITUDE VARIATION WITH OFFSET APPROXIMATION

The physical processes and interaction between the pore-fluid phase and rock-solid phase in homogeneous porous media were first explained by Biot (1941) and Gassmann (1951). The Biot-Gassmann theory accurately predicts seismic velocities as a function of fluid content and has remained the most robust and frequently implemented way to perform fluid substitution (Russell et al., 2003).

Based on the Biot-Gassmann theory, we get the following relationships in porous elastic media (Krief et al., 1990):

$$\lambda_{\text{sat}} = \lambda_{\text{dry}} + \beta^2 M, \tag{1}$$

$$K_{\text{sat}} = K_{\text{dry}} + \beta^2 M, \tag{2}$$

and

$$\mu_{\text{sat}} = \mu_{\text{dry}} = \mu, \tag{3}$$

where λ_{sat} and λ_{dry} are the first Lamé parameter values for the saturated and dry porous rock, K_{sat} and K_{dry} are the bulk modulus values for the saturated and dry porous rock, μ_{sat} and μ_{dry} are the second Lamé parameter values (shear modulus) for the saturated and dry porous rock, β is the Biot coefficient, and M is the modulus representing the pressure needed to force water into the formation without changing the cube volume. Equating Gassmann (1951) to Biot (1941), the parameters β and M in equations 1–3 can be expressed using bulk modulus as

$$\beta = 1 - \frac{K_{\text{dry}}}{K_s} \tag{4}$$

and

$$\frac{1}{M} = \frac{\beta - \phi}{K_s} + \frac{\phi}{K_f}, \tag{5}$$

where K_s is the bulk modulus of the solid grain, ϕ is the porosity of the porous rock, and K_f is the bulk modulus of the pore fluid. If there are multiple fluid phases in the pore, K_f is the effective pore-fluid bulk modulus, computed by the harmonic average $(1/K_f) = (S_1/K_{f_1}) + (S_2/K_{f_2}) + \cdots + (S_n/K_{f_n})$, where S_i is the saturation of fluid component K_{fi} and $i = 1, 2, \ldots, n$.

Based on the Biot-Gassmann theory (Biot, 1941; Gassmann, 1951), Russell et al. (2003) rewrite the P- and S-wave velocity expressions for the saturated porous rock as

$$V_{\text{P}} = \sqrt{\frac{f + s}{\rho_{\text{sat}}}} \tag{6}$$

and

$$V_{\text{S}} = \sqrt{\frac{\mu}{\rho_{\text{sat}}}}, \tag{7}$$

where V_{P} and V_{S} are the P- and S-wave velocities for the saturated porous rock, respectively; ρ_{sat} is the density of the saturated porous rock; s is a dry skeleton term, which can be written either as $\lambda_{\text{dry}} + 2\mu$ or $K_{\text{dry}} + (4/3)\mu$; and f is a mixed fluid/porosity term, which is written as $\beta^2 M$.

Based on equations 6 and 7, Russell et al. (2003) propose the fluid indicator $\rho f = I_{\text{P}}^2 - cI_{\text{S}}^2$, where $c = (V_{\text{P}}/V_{\text{S}})_{\text{dry}}^2$. In Russell et al. (2011), the mixed fluid/porosity term f was estimated directly to discriminate the pore-fluid types, in which the density effect was decoupled using a three term AVO approximation. By examining models and real data sets, the fluid/porosity term f has shown sensitivity to different pore-fluid types in various clastic reservoirs (Batzle et al., 2001; Zhang et al., 2009; Russell et al., 2011). However, as shown in equation 8, we note that the mixed fluid/porosity term f depends on many parameters, and although the fluid component plays a dominant role, the rock-matrix terms, namely the rock porosity, bulk modulus of dry rock and grain, will also influence f:

$$f = \beta^2 M = \frac{(1 - [K_{\text{dry}}/K_s])^2}{([\phi/K_f] + [(1-\phi)/K_s] - [K_{\text{dry}}/K_s^2])}. \tag{8}$$

To see the impact of the fluid component and rock-matrix component in the mixed fluid/porosity term f, we designed a rock model saturated with water and gas, in which we assumed that the water saturation ranges from 0% to 100% and the porosity ranges from 0% to 40%. Using this model, we calculated the logarithmic value of f for different pore-fluid saturations and rock porosities. The result is shown in Figure 1. We see that a model with high gas saturation and low porosity can have the same value

of f as one with high water saturation and high porosity, which means the f value does not change linearly with pore-fluid type and the effect of porosity. Therefore, it is not easy to identify fluid types if we only use f. This problem is addressed by Zhang et al. (2010). Next, we plot the variation of the effective pore-fluid bulk modulus K_f over the same pore-fluid saturation and porosity range. This is shown in Figure 2, and we see that the value of K_f varies linearly with water saturation, indicating that K_f depends entirely on the pore-fluid type. Thus, K_f is a more sensitive fluid indicator and can be used to diminish the ambiguity caused by porosity and other rock-matrix parameters.

Based on the Gassmann equation, Han and Batzle (2003) also estimate the pore-fluid bulk modulus as a fluid indicator from the log data. As shown in Appendix A, we can replace the fluid/porosity term f in Russell et al. (2003) AVO approximation with the term $G(\phi)$ derived by Han and Batzle (2003), as follows:

$$f = G(\phi)K_f, \tag{9}$$

where $G(\phi) = (1 - K_n)^2/\phi$ and $K_n = (K_{\text{dry}}/K_s)$. The $G(\phi)$ is called the gain function and is a property of the dry rock frame.

Using the critical porosity model proposed by Nur et al. (1998), we can reparameterize the Russell equation further and derive the new expression containing K_f, which we call the fluid-matrix decoupled AVO approximation. The final approximation is written as

$$\begin{aligned} R_{PP}(\theta) = &\left[\left(1 - \frac{\gamma^2_{\text{dry}}}{\gamma^2_{\text{sat}}}\right)\frac{\sec^2\theta}{4}\right]\frac{\Delta K_f}{\overline{K_f}} \\ &+ \left[\frac{\gamma^2_{\text{dry}}}{4\gamma^2_{\text{sat}}}\sec^2\theta - \frac{2}{\gamma^2_{\text{sat}}}\sin^2\theta\right]\frac{\Delta f_m}{\overline{f_m}} + \left[\frac{1}{2} - \frac{\sec^2\theta}{4}\right]\frac{\Delta\rho}{\overline{\rho}} \\ &+ \left(\frac{\sec^2\theta}{4} - \frac{\gamma^2_{\text{dry}}}{2\gamma^2_{\text{sat}}}\sec^2\theta + \frac{2}{\gamma^2_{\text{sat}}}\sin^2\theta\right)\frac{\Delta\phi}{\overline{\phi}}, \end{aligned} \tag{10}$$

where $f_m = \phi\mu$, which is a dry rock matrix term; ΔK_f, Δf_m, $\Delta\rho$, and $\Delta\phi$ are the differences of the average effective fluid bulk modulus, dry rock matrix term, density, and porosity values across the reflector; $\overline{K_f}$, $\overline{f_m}$, $\overline{\rho}$, and $\overline{\phi}$ are the average effective fluid bulk modulus, dry rock matrix term, density, and porosity values across the reflector; θ is the average of the incident and refracted angles; and γ^2_{sat} and γ^2_{dry} are the square of the P- to S-wave velocities of the saturated rock and dry rock, respectively.

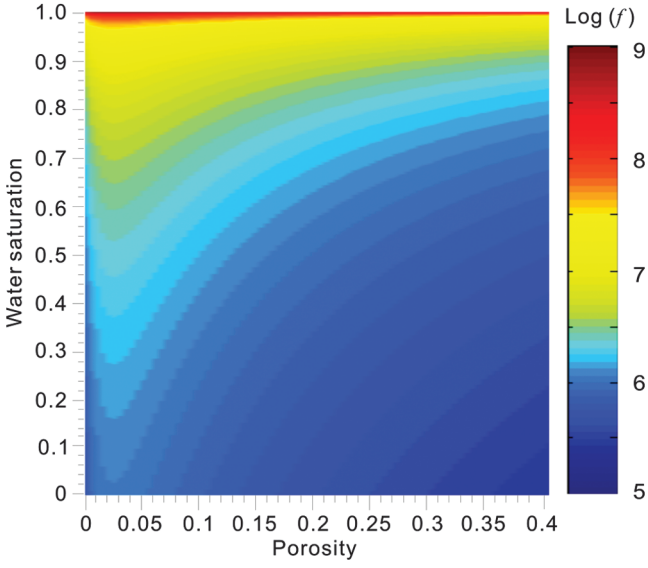

Figure 1. Fluid/porosity term f versus porosity and water saturation (the pore fluid is gas and water).

Note that there are four terms in the above approximation. Similar to the Russell equation, the saturated and dry rock V_P/V_S ratios squared (γ^2_{sat} and γ^2_{dry}) are the weighting coefficients in front of the reflectivity terms. If $\gamma^2_{\text{dry}} = \gamma^2_{\text{sat}}$, the weighting coefficient in front of $(\Delta K_f/\overline{K_f})$ becomes zero, which leaves only three terms. This means there is no pore-fluid component in the reservoir. Concerning the value of γ^2_{dry} of the equation, Russell et al. (2003, 2011) discuss how to estimate γ^2_{dry} based on lab measurements and real calculations, and they propose a range of values for γ^2_{dry} and the associated elastic parameters, as shown in Table 1. From the table, we see γ^2_{dry} ranges from 4 to 1.333. However, the value of 2 and 1.333

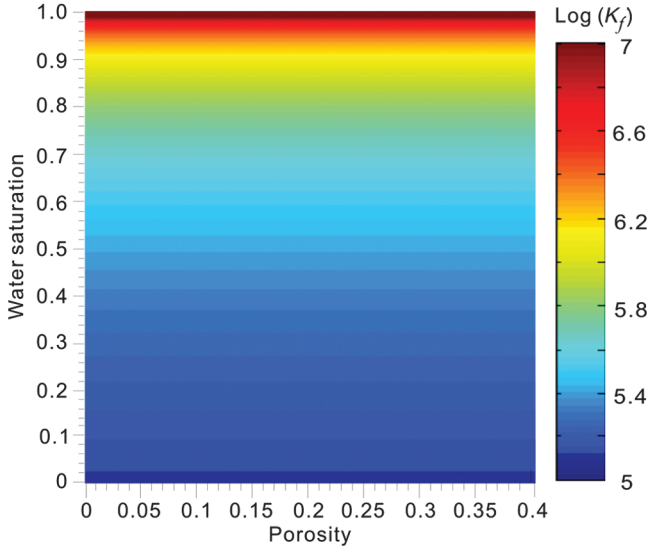

Figure 2. Effective pore-fluid bulk modulus K_f versus porosity and water saturation (the pore fluid is gas and water).

Table 1. Values for dry rock V_P/V_S ratio squared, dry rock V_P/V_S ratio, dry rock Poisson's ratio σ_{dry}, dry rock first Lamé parameter over shear modulus λ_{dry}/μ, and dry rock bulk modulus over shear modulus K_{dry}/μ (Russell et al., 2011).

γ^2_{dry}	γ_{dry}	σ_{dry}	$\frac{\lambda_{\text{dry}}}{\mu}$	$\frac{K_{\text{dry}}}{\mu}$
4.000	2.000	0.333	2.000	2.667
3.333	1.826	0.286	1.333	2.000
3.000	1.732	0.250	1.000	1.677
2.500	1.581	0.167	0.500	1.167
2.333	1.528	0.125	0.333	1.000
2.233	1.494	0.095	0.233	0.900
2.000	1.414	0.000	0.000	0.667
1.333	1.155	−1.000	−0.677	0.000

imply the dry rock Poisson's ratio of 0 and −1, neither of which is physically realistic for porous rock. Russell et al. (2003, 2011) propose that the value of 2.333 is more appropriate for clean unconsolidated sandstones. However, considering the dependence of γ^2_{dry} on the reservoir being studied, the value should be locally derived, if possible.

Next, we analyze the weighting coefficients for reflectivity terms with different properties, that is, the terms $(\Delta K_f/\overline{K_f})$, $(\Delta f_m/\overline{f_m})$, $(\Delta\rho/\overline{\rho})$, and $(\Delta\phi/\overline{\phi})$, in equation 10. In our analysis, we assume that the incident angle ranges from 0° to 60°, whereas γ^2_{sat} is four and γ^2_{dry} is 2.333, 2.000, and 1.333, respectively. Figure 3a and 3b shows the weighting coefficients for $(\Delta K_f/\overline{K_f})$ and $(\Delta f_m/\overline{f_m})$. We see that, with the increase of γ^2_{dry}, the weighting coefficients for $(\Delta K_f/\overline{K_f})$ move closer to zero, and weighting coefficients for $(\Delta f_m/\overline{f_m})$ move further away from zero. Figure 3a and 3b shows that, as γ^2_{dry} decrease for a fixed γ^2_{sat}, the $(\gamma^2_{\text{dry}}/\gamma^2_{\text{sat}})$ ratio increases its effect on $(\Delta K_f/\overline{K_f})$, but reduces its effect on $(\Delta f_m/\overline{f_m})$, which is similar to the trends shown in the weighting coefficients for $(\Delta f/\overline{f})$ and $(\Delta\mu/\overline{\mu})$ in the Russell et al. (2011) equation. Figure 3c shows the weighting coefficients for $(\Delta\rho/\overline{\rho})$, in which the value of the weighting coefficients is positive at angles less than 45°, equals zero at 45°, and becomes negative at angles greater than 45°. As expected, the coefficients of the three different cases coincide with each other due to the fact that the density term does not depend on $(\gamma^2_{\text{dry}}/\gamma^2_{\text{sat}})$ and it is only a function of $\sec^2\theta$. Figure 3d shows the weighting coefficients for $(\Delta\phi/\bar{\phi})$. We note that the weighting coefficient increases as the value of γ^2_{dry} decreases, which means the value of $(\gamma^2_{\text{dry}}/\gamma^2_{\text{sat}})$ also has an effect on $(\Delta\phi/\bar{\phi})$.

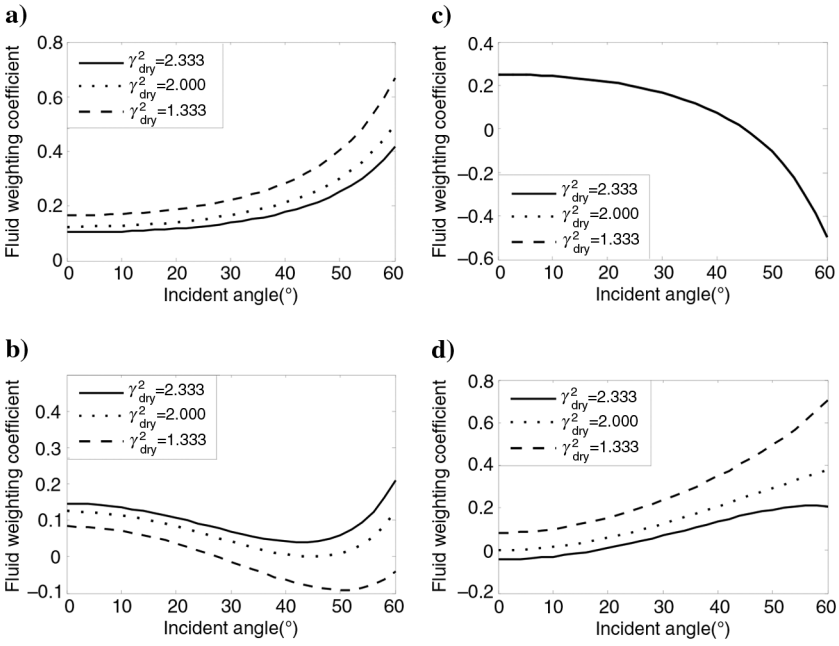

Figure 3. (a) Weighting coefficients for $\Delta K_f/K_f$ of three different dry rock velocity ratio cases, (b) weighting coefficients for $\Delta f_m/f_m$ of three different dry rock velocity ratio cases, (c) weighting coefficients for $\Delta\rho/\rho$ of three different dry rock velocity ratio cases, and (d) weighting coefficients for $\Delta\phi/\phi$ of three different dry rock velocity ratio cases. And these three cases are $\gamma^2_{\text{dry}} = 2.333$ (solid line), $\gamma^2_{\text{dry}} = 2.000$ (dotted line), and $\gamma^2_{\text{dry}} = 1.333$ (dashed line).

MODEL EXAMPLES

We created three models to test the accuracy of equation 10. The values of the elastic parameters in these three models are shown in Table 2. The three models all consist of two sand layers overlaying each other and have the same solid grain in the rock frame. In model 1, the top sand was fully gas saturated with $K_f = 0.10$ GPa and the underlying sand was fully water saturated with $K_f = 2.38$ GPa. The porosity of each sand layer was set equal to 25%. The only difference between the two sand layers is the pore-fluid type. In model 2, the top layer was fully water saturated and the porosity was kept at 25%. Therefore, the elastic parameters for the top layer were identical to the underlying layer of model 1. The underlying sand layer of model 2 was also fully water saturated. However, the porosity of underlying layer was set to 20% that means the difference between the two layers of model 2 was only the porosity. In model 3, pore fluid and porosity were modeled with different values. The top layer was gas saturated, with the value of $K_f = 0.10$ GPa, and the underlying layer was water saturated, with a value of $K_f = 2.38$ GPa, which is the same pore-fluid types as in model 1. However, the porosities of the top layer and underlying layer were modeled a 20% and 25%,

Table 2. Values of three sand models.

		K_f (Gpa)	K_{dry} (Gpa)	K_s (Gpa)	μ (Gpa)	ρ (kg/cm^3)	V_{P} (km/s)	V_{S} (km/s)	Φ (-)
Model 1	Gas sand	0.10	3.00	40.0	3.00	1.99	1.92	1.23	25%
	Water sand	2.38	3.00	40.0	3.00	2.26	2.59	1.15	25%
Model 2	Water sand	2.38	3.00	40.0	3.00	2.26	2.59	1.15	25%
	Water sand	2.38	10.0	40.0	10.0	2.34	3.58	2.07	20%
Model 3	Gas sand	0.10	10.0	40.0	10.0	2.12	3.34	2.17	20%
	Water sand	2.38	3.0	40.0	3.00	2.26	2.59	1.15	25%

respectively. Based on Biot-Gassmann poroelastic theory and fluid substitution methodology, we estimated the corresponding values of P- and S-wave velocities and density in each layer, as shown in Table 2. We used equation 10 to calculate AVO curve at the interface of these three models, and compared them with the curves computed using the Zoeppritz equation and the Aki-Richards approximation. The comparisons of the AVO curves are shown in Figure 4.

In model 1, the four reflectivities in equation 10 are calculated as $(\Delta K_f/\overline{K_f}) = 1.839$, $(\Delta f_m/\overline{f_m}) = 0$, $(\Delta\rho/\bar{\rho}) = 0.127$, and $(\Delta\phi/\bar{\phi}) = 0$. Because the rock grain bulk modulus and porosity are the same for the top and underlying layers, the reflectivities of dry rock matrix term and porosity are zero. The change of pore fluid makes a difference between the densities of the layers, although the density reflectivity is quite small. The P- and S-wave velocity reflectivities are $(\Delta V_P/\overline{V_P}) = 0.297$ and $(\Delta V_S/\overline{V_S}) = -0.067$. As shown in Figure 4a, the AVO curve computed from equation 10 is very close to the ones computed from the Zoeppritz equation and the Aki-Richards approximation. That is because the derivation of equation 10 starts from the Aki-Richards approximation, and thus both equations give similar AVO curves. Because the AVO approximations are valid under the assumption of small elastic parameter perturbations across the reflectors, the small changes in P-wave velocity, S-wave velocity, and density caused by only pore fluid change make both our approximation and the Aki-Richards approximation close to the Zoeppritz equation.

In model 2, the four reflectivities in equation 10 are calculated as $(\Delta K_f/\overline{K_f}) = 0$, $(\Delta f_m/\overline{f_m}) = 0.909$, $(\Delta\rho/\bar{\rho}) = 0.035$, and $(\Delta\phi/\bar{\phi}) = -0.222$. Because the two layers are saturated with the same pore fluid, the effective pore-fluid bulk modulus reflectivity is zero. Due to the change of the porosity, the dry rock matrix term and the density are different between the top and underlying layers, and the relative change of f_m is larger than the change of ρ. We note that the porosity-change effect in this model is still less than the fluid-change effect in the first model. However, the P- and S-wave velocity reflectivities are $(\Delta V_P/\overline{V_P}) = 0.321$ and $(\Delta V_S/\overline{V_S}) = 0.571$, of which are larger than $(\Delta V_P/\overline{V_P})$ and $(\Delta V_S/\overline{V_S})$ in the first model. As shown in Figure 4b, the AVO curves computed from the Aki-Richards approximation and equation 10 are almost identical, and both curves are close to the Zoeppritz curve for incident angles less than 35°. However, with an increase of incident angle, the AVO curves computed from Aki-Richards approximation and equation 10 diverge from the Zoeppritz curve. This is because the effect of porosity on the velocities is greater than the effect of pore fluid. Therefore, the porosity difference creates larger change in P- and S-wave velocities across the interface, which produces a larger error between the AVO approximation and exact Zoeppritz equation for large incident angles.

In model 3, the reflectivities in equation 10 are calculated as $(\Delta K_f/\overline{K_f}) = 1.839$, $(\Delta f_m/\overline{f_m}) = -0.909$, $(\Delta\rho/\bar{\rho}) = 0.0639$, and $(\Delta\phi/\bar{\phi}) = 0.222$. Because the pore fluid and porosity change between the top layer and the underlying layer, all four reflectivity values are nonzero, and the changes of the four terms are the largest of the three models. The P- and S-wave velocity reflectivities are $(\Delta V_P/\overline{V_P}) = -0.253$ and $(\Delta V_S/\overline{V_S}) = -0.615$. In Figure 4d, note that the AVO curves computed from equation 10 and the Aki-Richards approximation are nearly identical, and both are very close to the Zoeppritz curve for an incident angle range of less than 35°. However, for larger incident angles, the misfit between the two curves and the Zoeppritz curve becomes larger. That is because the large changes of P- and S-wave velocities caused by changes in fluid content and porosity make the AVO approximations less valid at large incident angles, as with model 2.

Because the range of incident angles used in the real seismic application is usually less than 40°, equation 10 is a reasonable approximation. If we extract rock properties using this new equation, the reconstructed amplitudes should match the seismic observations

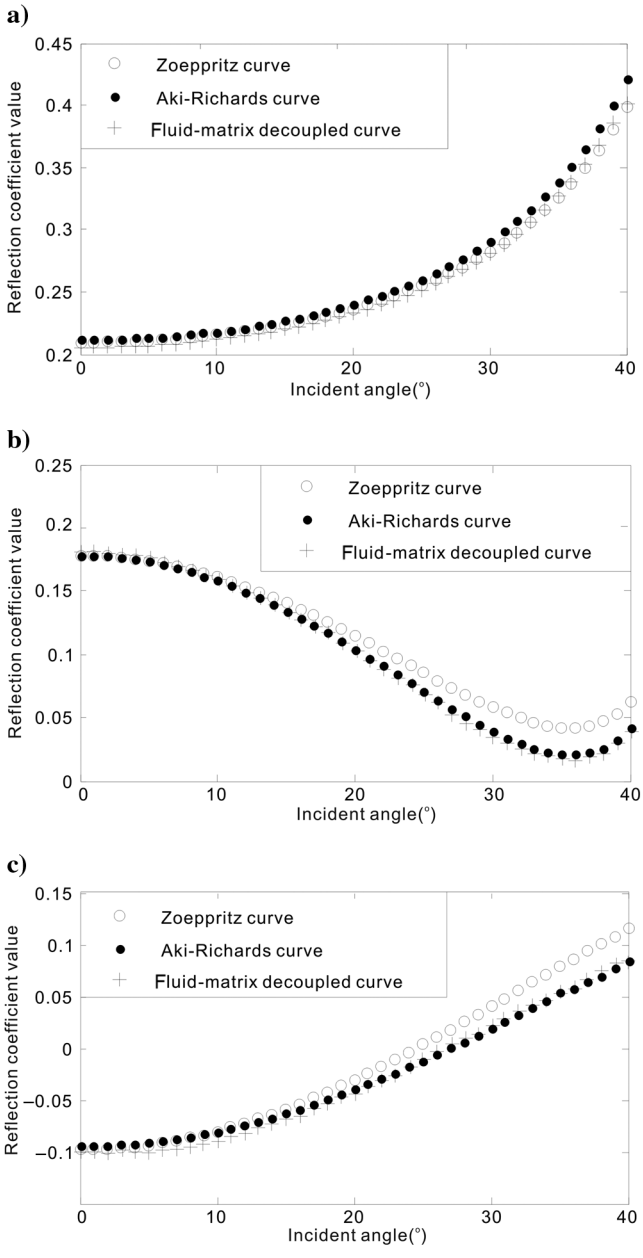

Figure 4. (a) A comparison between the curves derived from the exact Zoeppritz equation (circle), Aki-Richard equation (point), and fluid-matrix decoupled equation (plus) in model 1, (b) a comparison between the curves derived from the exact Zoeppritz equation (circle), Aki-Richard equation (point), and fluid-matrix decoupled equation (plus) in model 2, and (c) a comparison between the curves derived from the exact Zoeppritz equation (circle), Aki-Richard equation (point) and fluid-matrix decoupled equation (plus) in model 3.

relatively closely. However, this accuracy analysis is based on a simple two layer model with no noise. In real applications, the lack of perfect knowledge of the incident angle and dry and saturated velocity ratios will degrade the inversion results.

BAYESIAN INVERSION FOR EFFECTIVE PORE-FLUID BULK MODULUS

Using the fluid-matrix decoupled AVO approximation just derived, we can invert for the effective pore-fluid bulk modulus and use it as a fluid indicator to identify hydrocarbon reservoirs. Before we describe our inversion approach, we will discuss the mathematical forward model, which will play an important role in the inverse problem.

Equation 10 can be reexpressed as follows:

$$R_{PP}(\theta) = ar_{K_f} + br_{f_m} + cr_\rho + dr_\phi, \tag{11}$$

where $a = (1 - [\gamma_{\text{dry}}^2/\gamma_{\text{sat}}^2])(\sec^2\theta/4)$, $b = (\gamma_{\text{dry}}^2/4\gamma_{\text{sat}}^2)\sec^2\theta - (2/\gamma_{\text{sat}}^2)\sin^2\theta$, $c = (1/2) - (\sec^2\theta/4)$, $d = (\sec^2\theta/4) - (\gamma_{\text{dry}}^2/2\gamma_{\text{sat}}^2)\sec^2\theta + (2/\gamma_{\text{sat}}^2)\sin^2\theta$, $r_{K_f} = (\Delta K_f/\overline{K_f})$, $r_{f_m} = (\Delta f_m/\overline{f_m})$, $r_\rho = (\Delta\rho/\overline{\rho})$, and $r_{K_f} = (\Delta\phi/\overline{\phi})$.

Using equation 11, we can derive the matrix equation below for multiple offsets:

$$\begin{bmatrix} R(\theta_1) \\ R(\theta_2) \\ \vdots \\ R(\theta_m) \end{bmatrix} = \begin{bmatrix} a_1 & b_1 & c_1 & d_1 \\ a_2 & b_2 & c_2 & d_2 \\ \vdots & \vdots & \vdots & \vdots \\ a_m & b_m & c_m & d_m \end{bmatrix} \begin{bmatrix} r_{K_f} \\ r_{f_m} \\ r_\rho \\ r_\phi \end{bmatrix}, \tag{12}$$

where the subscript $i (i = 1, 2, \ldots, m)$ refers to the ith incident angle θ_i. Note that we need at least four angle traces for equation 12 to be fully invertible.

If we consider n samples for each seismic trace, the matrix expression 12 can be changed to

$$\begin{bmatrix} \mathbf{R_1} \\ \mathbf{R_2} \\ \vdots \\ \mathbf{R_m} \end{bmatrix} = \begin{bmatrix} \mathbf{A_1} & \mathbf{B_1} & \mathbf{C_1} & \mathbf{D_1} \\ \mathbf{A_2} & \mathbf{B_2} & \mathbf{C_2} & \mathbf{D_2} \\ \vdots & \vdots & \vdots & \vdots \\ \mathbf{A_m} & \mathbf{B_m} & \mathbf{C_m} & \mathbf{D_m} \end{bmatrix} \begin{bmatrix} \mathbf{R_{K_f}} \\ \mathbf{R_{f_m}} \\ \mathbf{R}_\rho \\ \mathbf{R}_\phi \end{bmatrix}, \tag{13}$$

where $\mathbf{R}_i (i = 1, 2, \ldots, m)$ is the n element reflection coefficient column vector for the ith angle; $\mathbf{A}_i (i = 1, 2, \ldots, m)$; $\mathbf{B}_i (i = 1, 2, \ldots, m)$; and $\mathbf{C}_i (i = 1, 2, \ldots, m)$ are the $n \times n$ diagonal matrices, which contain the corresponding weighting coefficients for the ith angle; and $\mathbf{R}_{K_f}$, $\mathbf{R}_{f_m}$, $\mathbf{R}_\rho$, and $\mathbf{R}_\phi$ are the $n \times 1$ column vectors containing the corresponding reflectivities.

Finally, $\mathbf{W}$ is a wavelet matrix containing the extracted wavelet that is convolved with the reflectivity matrix of equation 13 to give

$$\begin{bmatrix} \mathbf{d}_1 \\ \mathbf{d}_2 \\ \vdots \\ \mathbf{d}_m \end{bmatrix} = \begin{bmatrix} \mathbf{WA}_1 & \mathbf{WB}_1 & \mathbf{WC}_1 & \mathbf{WD}_1 \\ \mathbf{WA}_2 & \mathbf{WB}_2 & \mathbf{WC}_2 & \mathbf{WD}_2 \\ \vdots & \vdots & \vdots & \vdots \\ \mathbf{WA}_m & \mathbf{WB}_m & \mathbf{WC}_m & \mathbf{WD}_m \end{bmatrix} \begin{bmatrix} \mathbf{R}_{K_f} \\ \mathbf{R}_{f_m} \\ \mathbf{R}_\rho \\ \mathbf{R}_\phi \end{bmatrix}, \tag{14}$$

where $\mathbf{d}_i (i = 1, 2, \ldots, m)$ is an $n \times 1$ column vector. Equation 14 is the forward model of one seismic gather and can be represented more compactly with the following expression:

$$\mathbf{d}_{mn\times 1} = \mathbf{G}_{mn\times 3n}\mathbf{m}_{3n\times 1}, \tag{15}$$

where $\mathbf{d}_{mn\times 1} = [\mathbf{d}_1 \quad \mathbf{d}_2 \quad \cdots \quad \mathbf{d}_m]^T$, $\mathbf{G} = \begin{bmatrix} \mathbf{WA}_1 & \mathbf{WB}_1 & \mathbf{WC}_1 & \mathbf{WD}_1 \\ \mathbf{WA}_2 & \mathbf{WB}_2 & \mathbf{WC}_2 & \mathbf{WD}_2 \\ \vdots & \vdots & \vdots & \vdots \\ \mathbf{WA}_m & \mathbf{WB}_m & \mathbf{WC}_m & \mathbf{WD}_m \end{bmatrix}$, and $\mathbf{m}_{3n\times 1} = [\mathbf{R}_{K_f} \quad \mathbf{R}_{f_m} \quad \mathbf{R}_\rho \quad \mathbf{R}_\phi]^T$ contain the rock properties to be estimated through the inversion process.

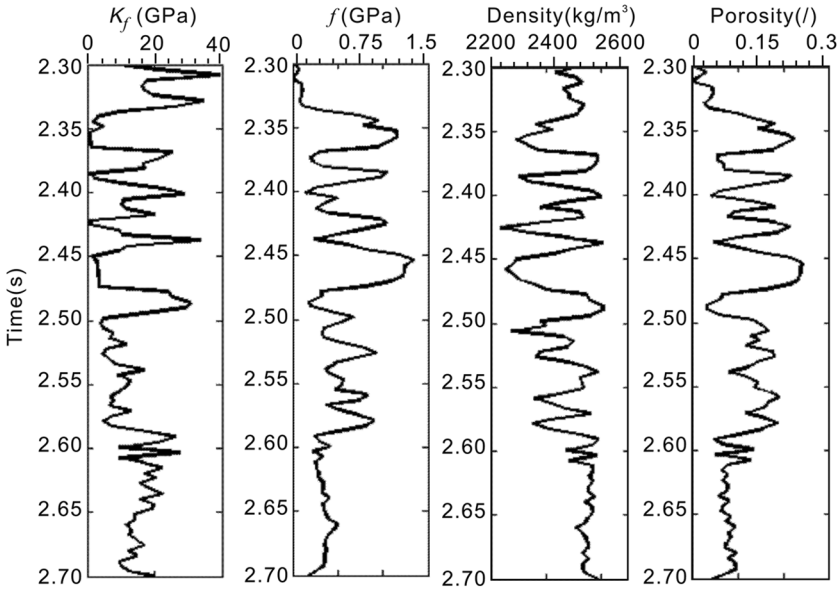

Figure 5. The real well-log data used as the test model.

In this study, we formulate the AVO inversion via a Bayesian inference framework (Ulrych et al., 2001). Based on the Bayesian rule, the posterior distribution for the rock properties is expressed as

$$P(\mathbf{m}|\mathbf{d}) = \frac{P(\mathbf{d}|\mathbf{m})P(\mathbf{m})}{P(\mathbf{d})}, \tag{16}$$

where $P(\mathbf{m})$ is the prior distribution that contains the general information about rock properties; $P(\mathbf{d}|\mathbf{m})$ is the likelihood function that defines the relationship between the observed seismic data and the subsurface rock properties; and $P(\mathbf{d})$ is the marginal probability distribution of the data, which is a constant value.

Assuming that the noise between the observed data and model is an uncorrelated normal distribution, the likelihood function is linearly Gaussian. We model the prior distribution of the inverted reflectivities as a Cauchy distribution, which will produce sparse results. Using the basic assumptions given above and substituting the

likelihood and prior distributions into equation 16, we get the following posterior model:

$$P(\mathbf{m}|\mathbf{d}) = \text{const}_o \times K_1 K_2 \exp\left[\frac{-(\mathbf{Gm}-\mathbf{d})^T(\mathbf{Gm}-\mathbf{d})}{2\sigma_n^2}\right] \cdot \prod_{i=1}^{N}\left[\frac{1}{1+m_i^2/\sigma_m^2}\right], \tag{17}$$

where const_o is a constant, which can be omitted from the next derivation; $K_1K_2 = \frac{1}{\sqrt{2\pi}\sigma_n} \cdot \frac{1}{(\pi\sigma_m)^N}$; N is the number of samples; σ_n is variance of the noise in the seismic data; $\sigma_m (m = 1, 2, 3, 4)$ is the variance of the reflectivities of subsurface rock properties; and the subscript refers to the four reflectivities given in equation 10.

By maximizing the posterior distribution and ignoring the constant values, we finally get the following objective function:

$$(\mathbf{G}^{\mathrm{T}}\mathbf{G} + \theta\mathbf{Q})\mathbf{m} = \mathbf{G}^{\mathrm{T}}\mathbf{d}, \tag{18}$$

where $\theta = (4\sigma_n^2/\sigma_1^2)$ and $\mathbf{Q}$ is a diagonal weighting matrix, which is defined as

$$Q_{ii} = \begin{cases} \frac{1}{\left(\frac{m_n'^2}{\sigma_1^2}+1.0\right)^2}, & i \le N \\ \frac{\sigma_1^2}{\sigma_2^2}\frac{1}{\left(\frac{m_n'^2}{\sigma_2^2}+1.0\right)^2}, & N < i \le 2N \\ \frac{\sigma_1^2}{\sigma_3^2}\frac{1}{\left(\frac{m_n'^2}{\sigma_3^2}+1.0\right)^2}, & 2N < i \le 3N \\ \frac{\sigma_1^2}{\sigma_4^2}\frac{1}{\left(\frac{m_n'^2}{\sigma_4^2}+1.0\right)^2}, & 3N < i \le 4N \end{cases}. \tag{19}$$

Using the iterative reweighed least-squares algorithm to solve equation 18 (Sacchi and Ulrych, 1995; Daubechies et al., 2010), we extract a sparse solution for the four reflectivities of the rock properties ($\Delta K_f/\overline{K_f}$, $\Delta f_m/\overline{f_m}$, $\Delta\rho/\overline{\rho}$, and $\Delta\phi/\overline{\phi}$). Using equation 20 below, we then compute the rock properties K_f, f_m, ρ, and ϕ:

$$\begin{cases} K_f(t) = K_f(t_0)\exp\left[2\int_0^t m_{K_f}(\tau)\mathrm{d}\tau\right], \\ f_m(t) = f_m(t_0)\exp\left[2\int_0^t m_{f_m}(\tau)\mathrm{d}\tau\right], \\ \rho(t) = \rho(t_0)\exp\left[2\int_0^t m_{\rho}(\tau)\mathrm{d}\tau\right], \\ \phi(t) = \phi(t_0)\exp\left[2\int_0^t m_{\phi}(\tau)\mathrm{d}\tau\right], \end{cases} \tag{20}$$

where t is the time samples and t_0 is the start time.

SYNTHETIC DATA TEST

To verify the feasibility and limitations of our inversion scheme from the previous section for the relevant elastic parameters, particularly the effective pore-fluid bulk modulus, we first use synthetic data to test the inversion. The synthetic angle gathers are generated by convolving the model reflectivity series with a 40 Hz Ricker wavelet. The four elastic properties used to calculate the reflectivity series are shown in Figure 5, in which the density and porosity curves are taken from a real well in the Bo Sea Field, and the effective pore-fluid bulk modulus and dry rock matrix values are calculated using well-log data and rock-physics theory (Makvo and Mukerji, 1995; Han and Batzle, 2003). The synthetic angle gathers are displayed in Figure 6a (with no noise added) and Figure 6b (with a signal-to-noise-ratio [S/N] equal to 1). The angle gather consists of 31 traces with incident angles ranging from 0° to 30°, in which the time sampling interval is 2 ms.

Figure 7 shows the elastic properties of the inversion of the synthetic data in Figure 6a. The real model elastic parameters are shown with solid lines and inverted elastic parameters are shown

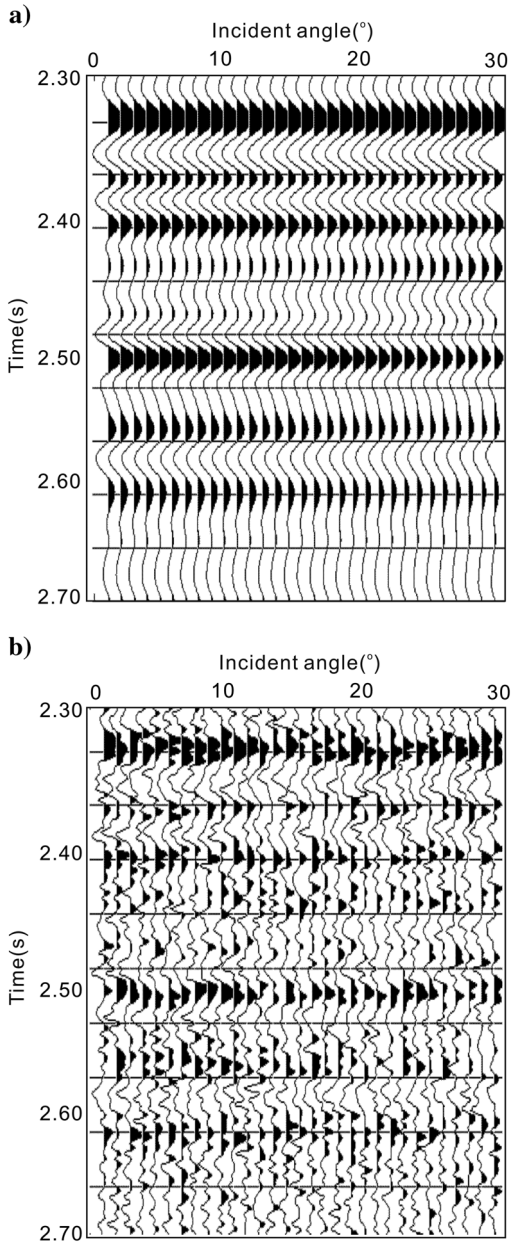

Figure 6. (a) The synthetic angle gather data without noise and (b) the synthetic angle gather data with noise added with an S/N of 1:1

with dash dot lines. We note that the inverted effective pore-fluid bulk modulus is close to the correct model values, with the largest error seen in the range of 2.47–2.57 s. The inverted dry rock matrix term and density are all close to the corresponding model data. The largest differences are seen between the inverted density and model density is especially in the range of 2.5–2.6 s. As a further test, the angle gather with added noise from Figure 6b is used to invert for the four elastic parameters and the results are displayed in Figure 8. Again, the solid lines represent the real model data and the dashed dotted lines represent the inverted parameters. The differences are relatively larger than in the noise free case of Figure 7. However, the error between the estimated effective pore-fluid bulk modulus and model value is not so severe that we can use it to identify hydrocarbon. The dry rock matrix term and density have a larger error than the inverted effective pore-fluid bulk modulus. The effect of the noise on the porosity shows the most serious misfit, and the inverted porosity is ambiguous for reservoir characterization in this case.

The synthetic test results reveal that it is difficult to estimate the porosity term using this inversion methodology. However, the other three elastic parameters can be inverted reliably. We think the reason is that the estimation of porosity in the AVO approximation is poor and its reliable estimation needs a more advanced inversion methodology. However, because that the purpose of this paper is to estimate the effective pore-fluid bulk modulus to produce a more sensitive fluid identification, we feel that our methodology has achieved our goal.

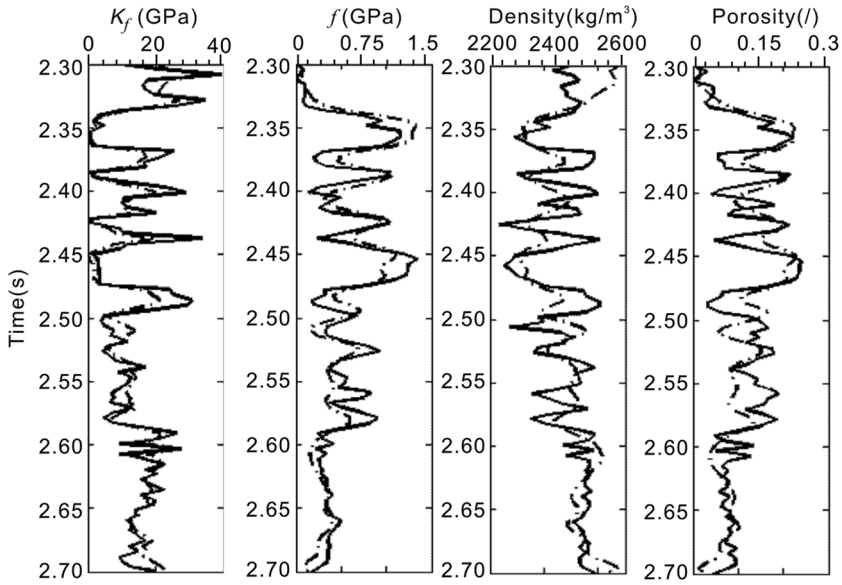

Figure 7. The inverted results from synthetic data with no noise added (the solid line indicates the model data, and the dashed dotted line indicates the inverted data).

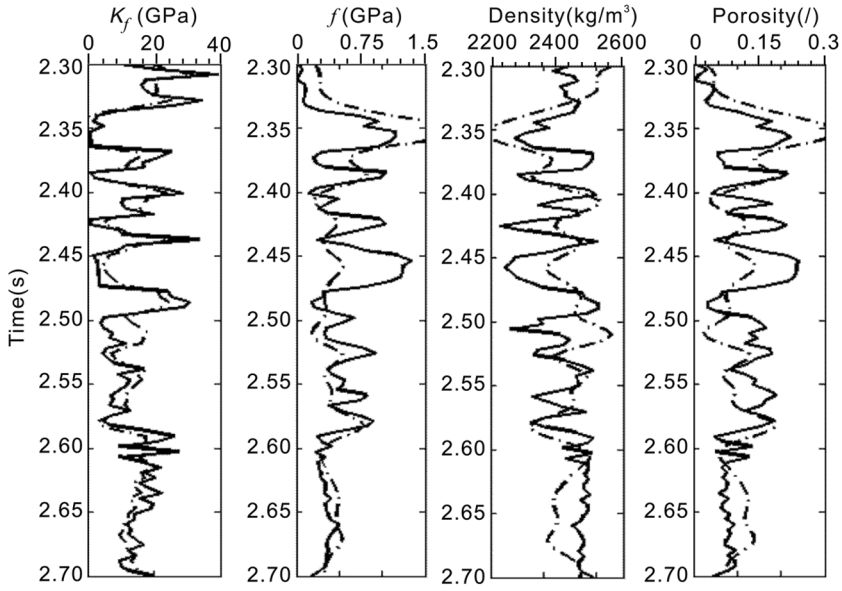

Figure 8. The inverted results from the synthetic data with noise added (the solid line indicates the model data, and the dashed dotted line indicates the inverted data).

REAL DATA APPLICATION

Bayesian inversion for effective pore-fluid bulk modulus and its validation in pore-fluid discrimination is next tested on a 2D seismic data set from a clastic basin in the Bo Sea, China. From our background knowledge of the geology of the area, we know that the target reservoir is delta front sheet sand that is controlled by structural and stratigraphic traps. The poststack seismic section of the test data is shown in Figure 9. Inserted into the poststack seismic section is the fluid interpretation of the well based on drilling results. In the inserted well, red indicates the gas sand, blue indicates the water sand, green indicates the oil sand, and white indicates everything else. As shown in Figure 9, the thick gas-saturated layer and the underlying thick water-saturated layer in the well correlate with a bright spot anomaly and structural high at 2.59 and 2.64 s, respectively, on the seismic section. Before the successful gas well was drilled, it was thought that both bright spot layers were hydrocarbon reservoirs based on the AVO analysis. However, the drill result proves that the overlying bright spot layer is a gas layer and the underlying spot layer is a water layer.

Based on the well-log data, we calculated several fluid indicators to test their sensitivity to the different pore fluids. Figure 10 shows the resistivity logging (Rt), density, and porosity curves and the estimated fluid indicators including the Gassmann fluid/porosity term f and the effective pore-fluid bulk modulus K_f. To account for the difference in the scales between the well log and the seismic, we upscale the well-log curves to the seismic scale in time domain. In Figure 10, the different pore-fluid types can be clearly indicated using the Rt curve. The Rt shows anomalously high values at the location of gas sand, but we note that the density and Gassmann fluid/porosity term f, which are the most common fluid

indicators, are still ambiguous in the discrimination of pore-fluid types. The density and fluid/porosity term show anomalously low values at the location of gas sand and water sand. However, it appears that the effective pore-fluid bulk modulus can differentiate between the gas sand and water sand because its value in the gas sand is smaller than in the water sand. From the porosity curve in Figure 10, we note that the porosity of the underlying water sand is larger than the overlying gas sand, which may be caused by the complex geology in the area. Considering the strong effect of rock porosity on fluid discrimination using common fluid indicators, we think that porosity may be the main cause of the ambiguous fluid identification.

Table 3 shows the mean value and standard deviation of the three fluid indicators, density, fluid/porosity term f, and effective pore-fluid bulk modulus K_f, for the gas and water sands. The fluid indicator coefficient is defined as the difference between the mean values of the gas and water sand divided by the standard deviation of the gas-sand attribute. The higher the value of the fluid indicator coefficient, the more sensitive is the discrimination between the gas and water sand. Note that the effective pore-fluid bulk modulus has the highest value of 119.583, and it is, therefore, the most sensitive discriminator between gas and water sands.

Prior to the estimation of elastic parameters using our proposed inversion method, we transform the 2D prestack test gathers from the time-offset domain to the time-angle domain. We choose the corresponding gathers with an incident angle ranging from 5° to 35°, determine the wavelet from the well-log data and seismic traces at the well location, and use this wavelet to construct the wavelet matrix in the inversion procedure. We then choose the density and effective pore-fluid bulk modulus from the inverted elastic parameters to use as fluid indicators and compare their fluid discrimination ability in this test data set. Figures 11 and 12 show the density and effective pore-fluid bulk modulus section, respectively. In both figures, we inserted the fluid interpretation well log (color blocky well), in which red indicates the gas sand, blue indicates the water sand, green indicates the oil sand, and white indicates everything else. Note that the effective pore-fluid bulk modulus and the density indicate the overlying gas-sand layer (with low porosity) and show good correlation with the fluid interpretation. Density cannot discriminate the underlying water-sand layer (with high porosity) from the overlying gas-sand layer (with low porosity), which has an overlap in values between the water sand and gas sand caused by porosity. However, the effective pore-fluid bulk modulus makes the difference between the gas layer and water layer more obvious and shows good correlation to the fluid interpretation.

Thus, this example shows that the effective pore-fluid bulk modulus can diminish the fluid discrimination ambiguity caused by porosity, and our method has proved to be an excellent fluid indicator to improve the quality of pore-fluid discrimination. Coupled with the Bayesian AVO inversion methodology, we have proposed here, we feel, we have developed a reliable method for estimating the pore-fluid bulk modulus.

DISCUSSION

In this study, we have developed a new AVO parameterization and a Bayesian inversion method to invert for the effective pore-fluid bulk modulus leading to pore-fluid discrimination. However, this study has several limitations. First, the effective pore-fluid bulk modulus is just an approximation to the real pore-fluid modulus and it might not indicate the real information of reservoir pore fluid. The reason that we chose the effective pore-fluid bulk modulus is that the effective medium theory is a powerful and robust tool to study the properties of the complex pore fluid variation in real rocks (Mavko et al., 1998). Through this analysis, we found that the effective pore-fluid bulk modulus is useful for indicating pore-fluid

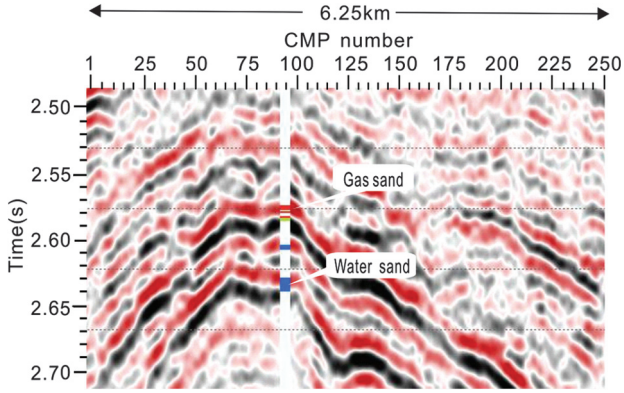

Figure 9. Poststack seismic section (colors), inserted fluid interpretation result using well logging interpretation (color blocky well). In the blocky well, red indicates the gas sand, blue indicates the water sand, green indicates the oil sand, and white indicates the others. The fluid type illustrations are shown in the location of the thick sand layer saturated with gas at 2.59 s and the thick layer saturated with water at 2.64 s, respectively. The gas layer and water layer exhibit bright spot anomalies at the location of structural high.

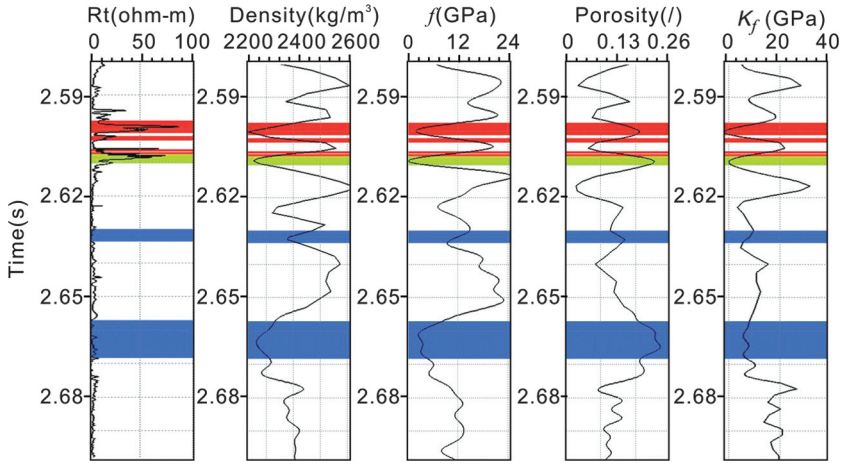

Figure 10. Well log and fluid indicator curves, including the Rt, density, fluid/porosity term f, porosity, and effective pore-fluid bulk modulus K_f. The curves of density, fluid/porosity term f, porosity, and effective pore-fluid bulk modulus K_f are transformed to seismic scale in time domain. The Rt curve can indicate the pore-fluid types that exhibit higher value in the gas-sand layer. The density and fluid/porosity term f has a similar value in the gas sand and water sand, which is caused by the anomalous variation of the porosity with depth. The effective pore-fluid bulk modulus K_f is unambiguous for the prediction of gas sand that is not affected by the porosity.

Table 3. Mean, standard deviation, and fluid indicator coefficient for the three fluid indicators (density, fluid/porosity term f, and effective pore-fluid bulk modulus K_f). The fluid indicator coefficient is defined as the difference between the attribute mean value related to gas and water sand divided by the standard deviation of the attribute related to the gas-sand reference.

Fluid indicator		ρ (kg/cm^3)	f (Gpa)	K_f (Gpa)
Gas sand	Mean value	2.284	2.906	0.857
	Std. dev.	0.041	0.365	0.048
Water sand	Mean value	2.283	7.698	6.597
	Std. dev.	0.016	4.322	0.287
Fluid indicator coefficient		0.024	13.129	119.583

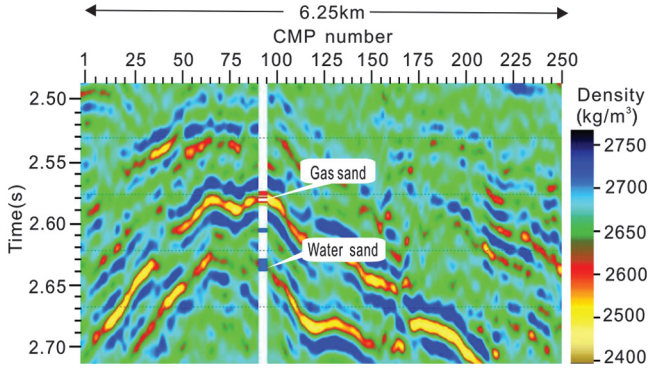

Figure 11. The inverted density term section (colors), inserted the fluid interpretation well log (color blocky well). In the blocky well, red indicates the gas sand, blue indicates the water sand, green indicates the oil sand, and white indicates the others. The fluid type illustrations are shown in the location of the two thick sand layers including gas and water, respectively. By the effect of porosity change, the value at the location of water-sand layer is similar to the value of gas sand, which makes the ambiguous fluid discrimination results.

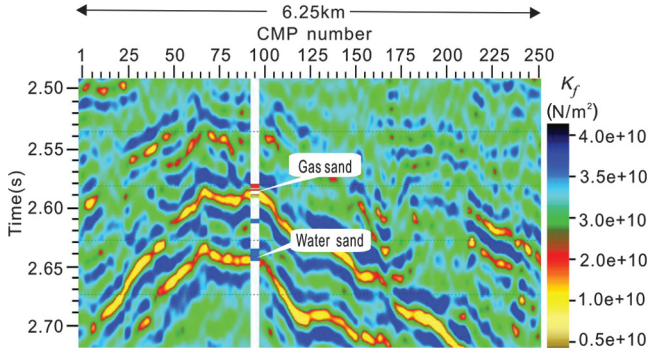

Figure 12. The inverted effective pore-fluid bulk modulus term section (colors), inserted the fluid interpretation well log (color blocky well). In the blocky well, red indicates the gas sand, blue indicates the water sand, green indicates the oil sand, and white indicates the others. The fluid type illustrations are shown in the location of the two thick sand layers including the gas and water, respectively. The gas-sand layer shows a lower value and the water-sand layer shows a higher value, which makes the difference between reservoirs saturated with different pore-fluid more obvious and lead to a reliable fluid discrimination result.

types. Second, the inversion proposed here is not robust in inverting for the porosity, which is also an important reservoir parameter. The inversion scheme we proposed can certainly be improved further to get a reliable estimate of the porosity term, which is important in reservoir characterization. However, considering that the focus of this paper is the estimation of effective pore-fluid bulk modulus, the inversion has achieved its purpose. Third, the critical porosity model is a good approximation for some clastic rocks but not for all rocks. In particular, it does not work if the rocks follow an inhomogeneous sorting trend. The extraction of effective pore-fluid bulk modulus in inhomogeneous reservoirs should be further researched. In short, the key goal of this paper was to estimate the effective pore-fluid bulk modulus from seismic data and we felt that we achieved this goal. We propose the use of effective pore-fluid bulk modulus as a more sensitive fluid indicator, which can lead to a more reliable hydrocarbon identification result in clastic reservoirs.

CONCLUSION

The effective pore-fluid bulk modulus can be used as a sensitive fluid indicator, which helps to diminish the fluid discrimination ambiguity caused by porosity. Using the poroelasticity AVO and corresponding rock physics theory, we have derived a new linearized AVO approximation, which we call the fluid-matrix decoupled approximation. This new approximation contains four terms (the effective pore-fluid bulk modulus, dry rock matrix, density, and porosity reflectivities with their weighting coefficients, respectively) that provide the basis for the estimation of the seismic scale effective pore-fluid bulk modulus from prestack seismic gathers. We show through model studies that the new AVO approximation meets accuracy requirements and can be applied to the real data.

We also present a Bayesian AVO inversion methodology for the estimation of the effective pore-fluid bulk modulus. Based on synthetic test and real clastic reservoir application examples, we show that the inversion methodology we propose here can estimate the effective pore-fluid bulk modulus reliably and robustly. As a fluid indicator, the effective pore-fluid bulk modulus can discriminate between the effects of fluid type and it produces a more reliable fluid discrimination result.

It should be pointed out that a limitation of this approach is that the new AVO approximation does not fit rocks without a sorting trend. Further research needs to be done on the extraction of effective pore-fluid bulk modulus in those inhomogeneous reservoirs.

ACKNOWLEDGMENTS

We would like to thank Z. Kui for inspiring discussions. This work is financially supported by the National Basic Research Program of China (973 program, grant 2013CB228604). We also thank J. Shragge and three anonymous reviewers for their constructive comments, which improved the quality of this paper.

APPENDIX A

NEW AVO APPROXIMATION DERIVATION

Using poroelasticity theory, Russell et al. (2011) derive the new AVO approximation given as

$$R_{PP}(\theta) = \left[\left(1 - \frac{\gamma_{\text{dry}}^2}{\gamma_{\text{sat}}^2}\right)\frac{\sec^2\theta}{4}\right]\frac{\Delta f}{\bar{f}} + \left[\frac{\gamma_{\text{dry}}^2}{4\gamma_{\text{sat}}^2}\sec^2\theta - \frac{2}{\gamma_{\text{sat}}^2}\sin^2\theta\right]\frac{\Delta\mu}{\bar{\mu}} + \left[\frac{1}{2} - \frac{\sec^2\theta}{4}\right]\frac{\Delta\rho}{\bar{\rho}}, \tag{A-1}$$

where Δf, Δf, and Δf are the differences of the mixed fluid/porosity term, shear modulus, and density values across the reflector; $\bar{f}$, $\bar{\mu}$, and $\bar{\rho}$ are the average mixed fluid/porosity term, shear modulus, and density values across the reflector; θ is the average of the incident and refracted angles; and γ_{sat}^2 and γ_{dry}^2 are the square of the P- to S-wave velocities of the saturated rock and dry rock, respectively.

Han and Batzle (2003) use $G(\phi)$ as the gain function to simplify the fixed fluid/porosity term f and derive pore fluid modulus as a hydrocarbon indicator from log data. The simplified equation was given as

$$f = G(\phi)K_f, \tag{A-2}$$

where $G(\phi) = ([1 - K_n]^2/\phi)$, $K_n = (K_{\text{dry}}/K_s)$, and the gain function $G(\phi)$ represents a property of dry rock frame.

Applying equation A-2 to equation A-1 gives the equation as

$$R_{PP}(\theta) = \left[\left(1 - \frac{\gamma_{\text{dry}}^2}{\gamma_{\text{sat}}^2}\right)\frac{\sec^2\theta}{4}\right]\frac{\Delta(G(\phi)K_f)}{\bar{f}} + \left[\frac{\gamma_{\text{dry}}^2}{4\gamma_{\text{sat}}^2}\sec^2\theta - \frac{2}{\gamma_{\text{sat}}^2}\sin^2\theta\right]\frac{\Delta\mu}{\bar{\mu}} + \left[\frac{1}{2} - \frac{\sec^2\theta}{4}\right]\frac{\Delta\rho}{\bar{\rho}}. \tag{A-3}$$

We use the relationship proposed by Nur et al. (1998) to substitute for the shear modulus μ. Nur et al. (1998) give the equation as

$$\begin{cases} K_{\text{dry}} = K_s\left(1 - \frac{\phi}{\phi_c}\right), \\ \mu_{\text{dry}} = \mu_s\left(1 - \frac{\phi}{\phi_c}\right), \end{cases} \tag{A-4}$$

where ϕ_c is the critical porosity, K_s and μ_s are the bulk modulus and shear modulus of the solid grain, respectively. Note that equation A-4 is a linear average. Mavko et al. (1998) show that this is a reasonable approximation, but other authors have proposed alternative bounds, such as the Reuss bound (Russell, 2013) and the lower Hashin-Shtrikman bound (Dvorkin and Nur, 1996).

We use equation $\mu_{\text{dry}} = \mu_s(1 - [\phi/\phi_c])$ to substitute shear modulus μ into equation A-3, the equation can be rearranged as

$$R_{PP}(\theta) = \left[\left(1 - \frac{\gamma_{\text{dry}}^2}{\gamma_{\text{sat}}^2}\right)\frac{\sec^2\theta}{4}\right]\left(\frac{\Delta G(\phi)}{\overline{G(\phi)}} + \frac{\Delta K_f}{\overline{K_f}}\right) + \left[\frac{\gamma_{\text{dry}}^2}{4\gamma_{\text{sat}}^2}\sec^2\theta - \frac{2}{\gamma_{\text{sat}}^2}\sin^2\theta\right]\left(\frac{\Delta\mu_s}{\overline{\mu_s}} + \frac{\Delta(\phi_c - \phi)}{\overline{\phi_c - \phi}}\right) + \left[\frac{1}{2} - \frac{\sec^2\theta}{4}\right]\frac{\Delta\rho}{\bar{\rho}}. \tag{A-5}$$

Substituting $K_{\text{dry}} = K_s(1 - [\phi/\phi_c])$ into $G(\phi)$ of equation A-5, rearranging equation A-5 gives

$$R_{PP}(\theta) = \left[\left(1 - \frac{\gamma_{\text{dry}}^2}{\gamma_{\text{sat}}^2}\right)\frac{\sec^2\theta}{4}\right]\frac{\Delta K_f}{\overline{K_f}} + \left[\frac{\gamma_{\text{dry}}^2}{4\gamma_{\text{sat}}^2}\sec^2\theta - \frac{2}{\gamma_{\text{sat}}^2}\sin^2\theta\right]\frac{\Delta\mu_s}{\overline{\mu_s}} + \left[\left(1 - \frac{\gamma_{\text{dry}}^2}{\gamma_{\text{sat}}^2}\right)\frac{\sec^2\theta}{4}\right]\frac{(\phi_c - \phi)\Delta\phi}{\overline{\phi(\phi_c - \phi)}} + \left[\frac{\gamma_{\text{dry}}^2}{4\gamma_{\text{sat}}^2}\sec^2\theta - \frac{2}{\gamma_{\text{sat}}^2}\sin^2\theta\right]\frac{\phi\Delta(\phi_c - \phi)}{\overline{\phi(\phi_c - \phi)}} + \left[\frac{1}{2} - \frac{\sec^2\theta}{4}\right]\frac{\Delta\rho}{\bar{\rho}}. \tag{A-6}$$

Note that $\frac{\phi\Delta(\phi_c-\phi)}{\overline{\phi(\phi_c-\phi)}} = \frac{\Delta[\phi(\phi_c-\phi)]}{\overline{\phi(\phi_c-\phi)}} - \frac{(\phi_c-\phi)\Delta\phi}{\overline{\phi(\phi_c-\phi)}}$ and apply this equation to rearrange equation A-6. Equation A-6 can be written as

$$R_{PP}(\theta) = \left[\left(1 - \frac{\gamma_{\text{dry}}^2}{\gamma_{\text{sat}}^2}\right)\frac{\sec^2\theta}{4}\right]\frac{\Delta K_f}{\overline{K_f}} + \left[\frac{\gamma_{\text{dry}}^2}{4\gamma_{\text{sat}}^2}\sec^2\theta - \frac{2}{\gamma_{\text{sat}}^2}\sin^2\theta\right]\frac{\Delta\mu_s}{\overline{\mu_s}} + \left[\frac{\sec^2\theta}{4} - \frac{\gamma_{\text{dry}}^2}{2\gamma_{\text{sat}}^2}\sec^2\theta + \frac{2}{\gamma_{\text{sat}}^2}\sin^2\theta\right]\frac{\Delta\phi}{\bar{\phi}} + \left[\frac{\gamma_{\text{dry}}^2}{4\gamma_{\text{sat}}^2}\sec^2\theta - \frac{2}{\gamma_{\text{sat}}^2}\sin^2\theta\right]\frac{\Delta[\phi(\phi_c - \phi)]}{\overline{\phi(\phi_c - \phi)}} + \left[\frac{1}{2} - \frac{\sec^2\theta}{4}\right]\frac{\Delta\rho}{\bar{\rho}}. \tag{A-7}$$

If

$$F_{\text{poro}} = \phi\mu_s(\phi_c - \phi),$$

then

$$F_{\text{poro}} = \phi\mu_s(\phi_c - \phi) = \phi_c\phi\mu_s\left(1 - \frac{\phi}{\phi_c}\right) = \phi_c\phi\mu. \tag{A-8}$$

Applying equation A-8 to equation A-7 gives

$$R_{PP}(\theta) = \left[\left(1 - \frac{\gamma_{\text{dry}}^2}{\gamma_{\text{sat}}^2}\right)\frac{\sec^2\theta}{4}\right]\frac{\Delta K_f}{\overline{K_f}} + \left[\frac{\gamma_{\text{dry}}^2}{4\gamma_{\text{sat}}^2}\sec^2\theta - \frac{2}{\gamma_{\text{sat}}^2}\sin^2\theta\right]\frac{\Delta(\phi\mu)}{\overline{\phi\mu}} + \left[\frac{1}{2} - \frac{\sec^2\theta}{4}\right]\frac{\Delta\rho}{\bar{\rho}} + \left(\frac{\sec^2\theta}{4} - \frac{\gamma_{\text{dry}}^2}{2\gamma_{\text{sat}}^2}\sec^2\theta + \frac{2}{\gamma_{\text{sat}}^2}\sin^2\theta\right)\frac{\Delta\phi}{\bar{\phi}}. \tag{A-9}$$

Equation A-9 is close to our final approximation. Here, we let $f_m = \phi\mu$, called the dry rock matrix term, which represents the

dry rock frame information. Applying f_m to equation A-9 gives the final fluid-matrix decoupled AVO approximation as

$$R_{PP}(\theta) = \left[\left(1-\frac{\gamma_{\rm dry}^2}{\gamma_{\rm sat}^2}\right)\frac{\sec^2\theta}{4}\right]\frac{\Delta K_f}{\overline{K_f}} + \left[\frac{\gamma_{\rm dry}^2}{4\gamma_{\rm sat}^2}\sec^2\theta - \frac{2}{\gamma_{\rm sat}^2}\sin^2\theta\right]\frac{\Delta(f_m)}{\overline{f_m}} + \left[\frac{1}{2}-\frac{\sec^2\theta}{4}\right]\frac{\Delta\rho}{\bar{\rho}} + \left(\frac{\sec^2\theta}{4} - \frac{\gamma_{\rm dry}^2}{2\gamma_{\rm sat}^2}\sec^2\theta + \frac{2}{\gamma_{\rm sat}^2}\sin^2\theta\right)\frac{\Delta\phi}{\bar{\phi}}. \quad \text{(A-10)}$$

REFERENCES

Alemie, W., and M. Sacchi, 2011, High-resolution three-term AVO inversion by means of a trivariate Cauchy probability distribution: Geophysics, **76**, no. 3, R43–R55, doi: 10.1190/1.3554627.

Batzle, M., D. Han, and R. Hofmann, 2001, Optimal hydrocarbon indicators: 71st Annual International Meeting, SEG, Expanded Abstracts, 1697–1700.

Biot, M. A., 1941, General theory of three-dimensional consolidation: Journal of Applied Physics, **12**, 155–164, doi: 10.1063/1.1712886.

Buland, A., and H. Omre, 2003, Bayesian linearized AVO inversion: Geophysics, **68**, 185–198, doi: 10.1190/1.1543206.

Castagna, J. P., M. L. Batzle, and R. L. Eastwood, 1985, Relationships between compressional-wave and shear-wave velocities in clastic silicate rocks: Geophysics, **50**, 571–581, doi: 10.1190/1.1441933.

Daubechies, I., R. DeVore, M. Fornasier, and C. S. Gunturk, 2010, Iteratively re-weighted least squares minimization for sparse recovery: Communications on Pure and Applied Mathematics, **63**, 1–38, doi: 10.1002/cpa.20303.

Dillon, L., G. Schwedersky, G. Vasquez, R. Velloso, and C. Nunes, 2003, A multiscale DHI elastic attributes evaluation: The Leading Edge, **22**, 1024–1029, doi: 10.1190/1.1623644.

Downton, J. E., 2005, Seismic parameter estimation from AVO inversion: Ph.D. thesis, University of Calgary.

Dvorkin, J., and A. Nur, 1996, Elasticity of high-porosity sandstones: Theory for two North Sea data sets: Geophysics, **61**, 1363–1370, doi: 10.1190/1.1444059.

Fatti, J. L., P. J. Vail, G. C. Smith, P. J. Strauss, and P. R. Levitt, 1994, Detection of gas in sandstone reservoirs using AVO analysis: A 3-D seismic case history using the geostack technique: Geophysics, **59**, 1362–1376, doi: 10.1190/1.1443695.

Gassmann, F., 1951, Über die Elastizitat poroser Medien: Vierteljahrsschrift der Naturforschenden Gesellschaft, **96**, 1–23.

Gidlow, P. M., G. C. Smith, and P. J. Vail, 1992, Hydrocarbon detection using fluid factor traces: A case history: How useful is AVO analysis?: Joint Summer Research Workshop, SEG/EAEG, Expanded Abstracts, 78–89.

Goodway, W. N., T. Chen, and J. Downton, 1997, Improved AVO fluid detection and lithology discrimination using Lamé petrophysical parameters; "λ," "μ," and "λ/μ fluid stack," from P and S inversions: 67th Annual International Meeting, SEG, Expanded Abstracts, 183–186.

Gray, F., T. Chen, and W. Goodway, 1999, Bridging the gap: Using AVO to detect changes in fundamental elastic constants: 69th Annual International Meeting, SEG, Expanded Abstracts, 852–855.

Han, D., and M. Batzle, 2003, Gain function and hydrocarbon indicators: 73rd Annual International Meeting, SEG, Expanded Abstracts, 1695–1698.

Krief, M., J. Garat, J. Stellingwerff, and J. Ventre, 1990, A petrophysical interpretation using the velocities of P and S waves: The Log Analyst, **13**, 355–369.

Mavko, G., and T. Mukerji, 1995, Seismic pore space compressibility and Gassmann's relation: Geophysics, **60**, 1743–1749, doi: 10.1190/1.1443907.

Mavko, G., T. Mukerji, and J. Dvorkin, 1998, Rock physics handbook: Cambridge University Press.

Nur, A., G. Mavko, J. Dvorkin, and D. Galmudi, 1998, Critical porosity: A key to relating physical properties to porosity in rocks: The Leading Edge, **17**, 357–362, doi: 10.1190/1.1437977.

Quakenbush, M., B. Shang, and C. Tuttle, 2006, Poisson impedance: The Leading Edge, **25**, 128–138, doi: 10.1190/1.2172301.

Russell, B., 2013, A Gassmann-consistent rock physics template: CSEG Recorder, **38**, no. 6, 22–30.

Russell, B., D. Hedlin, and D. Hampson, 2011, Linearized AVO and poroelasticity: Geophysics, **76**, no. 3, C19–C29, doi: 10.1190/1.3555082.

Russell, B., K. Hedlin, F. Hilterman, and L. Lines, 2003, Fluid-property discrimination with AVO: A Biot-Gassmann perspective: Geophysics, **68**, 29–39, doi: 10.1190/1.1543192.

Sacchi, M. D., and T. J. Ulrych, 1995, High-resolution velocity gathers and offset space reconstruction: Geophysics, **60**, 1169–1177, doi: 10.1190/1.1443845.

Smith, G. C., and P. M. Gidlow, 1987, Weighted stacking for rock property estimation and detection of gas: Geophysical Prospecting, **35**, 993–1014, doi: 10.1111/j.1365-2478.1987.tb00856.x.

Ulrych, T. J., M. D. Sacchi, and A. Woodbury, 2001, A Bayes tour of inversion: A tutorial: Geophysics, **66**, 55–69, doi: 10.1190/1.1444923.

Zhang, S., X. Yin, and F. Zhang, 2009, Fluid discrimination study from fluid elastic impedance (FEI): 79th Annual International Meeting, SEG, Expanded Abstracts, 2437–2441.

Zhang, S., X. Yin, and F. Zhang, 2010, Quasi fluid modulus for delicate lithology and fluid discrimination: 80th Annual International Meeting, SEG, Expanded Abstracts, 404–408.

Zhou, Z., and F. Hilterman, 2010, A comparison between methods that discriminate fluid content in unconsolidated sandstone reservoirs: Geophysics, **75**, no. 1, B47–B58, doi: 10.1190/1.3253153.